Computer Methods in Applied Mechanics and Engineering 419 (2024) 116580

Contents lists available at ScienceDirect

Computer Methods in Applied Mechanics and Engineering

journal homepage: www.elsevier.com/locate/cma

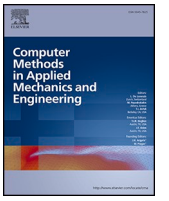

Coupled total- and semi-Lagrangian peridynamics for modelling fluid-driven fracturing in solids

Changyi Yang [a], Fan Zhu [c], Jidong Zhao [a,b,*]

[a] Department of Civil and Environmental Engineering, The Hong Kong University of Science and Technology, HKSAR, China
[b] HKUST Shenzhen-Hong Kong Collaborative Innovation Research Institute, Shenzhen 518045, PR China
[c] Department of Urban Management, Kyoto University, Kyoto, Japan

ARTICLE INFO

Keywords:
Peridynamics
Fluid-driven fracturing
Hydrodynamics
Fluid-solid interaction
Semi-lagrangian

ABSTRACT

This paper presents a novel computational approach for modelling fluid-driven fracturing in quasi-brittle solids using peridynamics. The approach leverages a rigorous coupling of the total- and semi-Lagrangian formulations of peridynamics. Specifically, the total-Lagrangian formulation, whch is based on classical peridynamics theory used for modelling fractures in solids, is combined with the semi-Lagrangian formulation to solve the Navier-Stokes equation using a non-local differential operator for weakly compressible fluid flow. The proposed approach offers a unified peridynamics-based framework that enables simulations of a wide range of fluid-driven fracturing problems in solids. The framework can model the solid as either an ordinary or non-ordinary material and quantify the fluid with different equations of state. To prevent unphysical inter-penetration, a fluid-solid interaction scheme that assumes fictitious fluid points in the solid domain is proposed to quantify the forces at the fluid-solid interface. The proposed computational approach is validated through simulations of several classic problems, including the dam break and the Kristianovich-Geertsma-de Klerk (KGD) problem. The predictive capability of the proposed approach is further demonstrated by numerical examples of fractures induced by fluid injection in sandstone, which reasonably capture the fracture patterns compared to experimental results. The presented approach offers an alternative to explicit modelling of fluid-driven fracturing processes and may find wide and useful applications to a variety of industrial and geophysical processes.

1. Introduction

Fluid-driven fractures are a common occurrence in both natural and industrial processes. For example, in volcanology, pressurized magma can cause fractures in the geological strata that eventually lead to eruptions. In the energy sector, hydraulic fracturing techniques are widely used to enhance oil production by injecting pressurized fluids into oil-bearing shales to create fractures and improve permeability [1]. Geologic sequestration of carbon dioxide is another application where the injection of gas or liquid CO_2 can trigger fractures that alter the permeability of the underground geological formation to mitigate carbon emissions [2]. Blasting can also be considered as a type of fluid-driven fracture, where high-temperature and high-pressure explosive gas triggers fractures in solids. Therefore, modelling fluid-driven fractures is relevant to many scientific studies and industrial applications. However, the associated

* Corresponding author.
E-mail address: jzhao@ust.hk (J. Zhao).

https://doi.org/10.1016/j.cma.2023.116580
Received 14 August 2023; Received in revised form 28 October 2023; Accepted 29 October 2023
Available online 16 November 2023
0045-7825/

challenges can be formidable, particularly when complex fracture patterns are present and complicated fluid-solid interaction (FSI) needs to be properly quantified.

Existing computational methods for modelling fluid-driven fractures include the finite element method (FEM) based approaches [3–8] where the fracturing process is handled with either extended FEM or cohesive elements, and meshfree methods such as discrete element method (DEM) [9–10], smoothed particle hydrodynamics (SPH) [11–12], and peridynamics (PD) [13–15]. Fluids within the crack are often modelled with Reynolds lubrication equation [16] in conjunction with the Poiseuille's law, where the former describes conservation of fluids within the crack and latter relates fluid influx with pressure. Alternatively, fluids can also be handled with simplified approaches, such as directly adding a pressure term into the momentum equations of solids [13] when modelling the propagation of fractures.

Peridynamics (PD) theory, introduced by Silling et al. [17–18] as an alternative formulation of classical continuum mechanics, has emerged as a promising approach for modelling discontinuities in solids. PD replaces the partial differential operator of the displacement field with an integral operator, making it inherently suitable for handling discontinuities such as fractures. As a particle-based method, PD models fractures through the damage of bonds that connect material points and does not require explicit description of the crack surface. This feature makes it particularly advantageous when modelling complex fracture patterns. PD has been successfully applied to simulate mechanically and thermally induced fractures, including concrete [19], glass [20], geomaterials [21–22], and composite materials [23]. A though review of benchmark studies of PD is provided in [24].

The early version of PD is known as bond-based peridynamics (BBPD), which is restricted to a micro-polar material model with a fixed Poisson's ratio of 0.25 [18]. Later, the state-based peridynamics (SBPD) largely overcame the drawbacks in BBPD, by postulating the force experienced by a bond dependant on not only the bond deformation but also the deformation at neighbouring bonds. SBPD can be further divided into ordinary and non-ordinary types. Ordinary SBPD is a pure peridynamic formulation of material, whereas non-ordinary SBPD approximates engineering stress and strain at the material points, offering convenience for implementing classical constitutive material models into the novel PD approach. PD theory has been extended to model fluid-driven fractures for various scenarios. For instance, Zhang et al. [15] employed ordinary SBPD to model hydraulic fracturing in rock-like materials by incorporating the fluid effect as a pressure term in the momentum equation in PD. To explicitly model both fluid and solid, immersed boundary method has been recently utilized to combine peridynamics with different mesh-based methods such as isogeometric analysis [25–27] and Lattice Boltzmann method [28]. A coupled SPH-PD approach was introduced by [29–31] for modelling jetting and blasting scenarios, where high-speed water and explosive gas are simulated by SPH while solids are simulated by PD. An apparent advantage of such approaches is that both solid and fluid are simulated by particle-based methods, so there is no need to explicitly describe the fracture geometry.

The classical PD theory uses a total-Lagrangian formulation to compute the material response based on a reference configuration, making it suitable for modelling small strain behaviour of solid materials. However, a new branch of PD theory, based on a semi-Lagrangian formulation, has been developed for modelling fluids [32–37]. This theory computes the material response based on the deformed configuration rather than the reference configuration, and is therefore often referred to as a semi-Lagrangian or Eulerian type of PD. The semi-Lagrangian PD formulation employs a non-local integral operator to replace the differential operators in the Navier-Stokes equation for modelling fluids. Another recent approach for modelling fluids based on the PD theory involves the use of the peridynamics differential operator introduced by Madenci et al. [38]. The peridynamics differential operator is designed to transform differential equations of any order from local to non-local form, by constructing PD functions of polynomials with unknown coefficients using Taylor series expansion. These coefficients can be determined analytically or numerically by solving a system of linear equations according to the orthogonality property of PD functions. Although initially regarded as a purely mathematical manipulation, the peridynamics differential operator has been successfully applied by [39–40] to simulate water flow problems. Gao and Oterkus [41] have proposed a coupled PD-peridynamics differential operator scheme for modelling fluid-structure interaction with simulation of a water column collapse. However, the peridynamics differential operator requires neighbour searching at each time step and must be constructed for each material point to enable the nonlocal form of local differential equations, making it computationally more expensive than the semi-Lagrangian PD method. Indeed, neither semi-Lagrangian PD nor peridynamics differential operator is fundamentally different from SPH, as both employ integrals rather than derivatives in their formulation. However, the semi-Lagrangian PD and peridynamics differential operator could offer a more consistent framework when coupling with the classical total-Lagrangian PD theory. For modelling fluid-driven fractures, coupling between the total- and semi-Lagrangian PD theories appears a promising approach since both solid and fluid can be solved within the same computational framework.

This study proposes a new approach for modelling fluid-driven fractures using a coupled total- and semi-Lagrangian PD approach. In this approach, fluids are modelled using the semi-Lagrangian formulation, while the solids with the classical total-Lagrangian formulation. A coupling algorithm is presented to quantify the FSI. The aim of this study is to develop a unified computational approach within the framework of peridynamics to handle both fluids, solids, and FSI. This paper is organized as follows: Section 2 provides an overview of the peridynamics theory, including the total- and semi-Lagrangian formulations. Section 3 presents the coupling algorithm for modelling FSI. Section 4 presents a series of numerical simulations based on the presented methodology, including dam break problem, crack profile under hydrostatic pressure, KGD problem for fluid-driven fractures, and rock fracturing due to hydraulic pressure. Finally, Section 5 presents a summary and conclusion.

2. Peridynamics theory

2.1. Total-Lagrangian formulation

PD models a continuum domain as discretized material points that interact through peridynamic bonds. The extent of such interaction is defined by a radius termed *horizon*. All material points within the *horizon* are called *neighbours* or *family* of the centring point. These concepts are illustrated in Fig. 1. In the present study the SBPD has been employed for simulating solid materials. The equation of motion in the SBPD writes

$$\rho_x \ddot{\boldsymbol{u}}_x = \int_{\Omega_x} [\boldsymbol{T} < \boldsymbol{x}' - \boldsymbol{x} > - \boldsymbol{T} < \boldsymbol{x} - \boldsymbol{x}' >] \mathrm{d}V_{x'} + \boldsymbol{b}_x \tag{1}$$

where ρ represents material density at a material point, $\boldsymbol{u}$ represents material point deformation, Ω_x defines the *family* of point $\boldsymbol{x}$, and $V_{x'}$ represents the volume of a neighbouring point. $\boldsymbol{b}$ denotes body force density. $\boldsymbol{T}$ is a force state that maps the bond deformation into bond force density. The angle brackets are used to indicate the vector on which a *state* operates. For example, $\boldsymbol{T}\langle \boldsymbol{x}' - \boldsymbol{x} \rangle$ represents the force state $\boldsymbol{T}$ operates on the vector $\boldsymbol{x}' - \boldsymbol{x}$, which physically denotes the force exerted by neighbouring point $\boldsymbol{x}'$ on master point $\boldsymbol{x}$. Similarly, $\boldsymbol{T}\langle \boldsymbol{x} - \boldsymbol{x}' \rangle$ can be interpreted as the force of master point $\boldsymbol{x}$ acting on neighbouring point $\boldsymbol{x}'$. The total bond force density at a material point is obtained by summarizing force densities of all neighbouring bonds. The integration presents a non-local approximation of the partial differential operator in classical continuum mechanics, and such feature makes the PD theory particularly suitable for modelling fracture related processes.

For an ordinary material, there exists a scalar force state t such that the force state of a bond $\boldsymbol{\xi} = \boldsymbol{x}' - \boldsymbol{x}$ can be computed by [18]

$$\boldsymbol{T}\langle \boldsymbol{x}' - \boldsymbol{x} \rangle = t \frac{\boldsymbol{Y}}{\| \boldsymbol{Y} \|} \tag{2}$$

where $\boldsymbol{Y}$ is the deformed bond vector, representing the magnitude of the bond force density. It is apparent that for all ordinary materials the bond force acts along the bond direction. In the present study, we adopt the linear peridynamic solid (LPS) model [18] to simulate elastic brittle materials. In the LPS model, the scalar force state is obtained by

$$t = \frac{3K\vartheta < \boldsymbol{x} >}{m < \boldsymbol{x} >} \omega < \|\boldsymbol{\xi}\| > \|\boldsymbol{\xi}\| + \frac{15\mu}{m < \boldsymbol{x} >} \boldsymbol{\omega} < \|\boldsymbol{\xi}\| > \underline{e}^{\mathrm{d}} \tag{3}$$

where K and μ are bulk and shear modulus, respectively. $\omega\langle \| \boldsymbol{\xi} \| \rangle$ is the value of influence function at bond $\boldsymbol{\xi}$. The influence function is selected in the form of a Gaussian function

$$\omega\langle \| \boldsymbol{\xi} \| \rangle = e^{-\left(\frac{\|\boldsymbol{\xi}\|}{\alpha\delta}\right)^2} \tag{4}$$

where δ denotes the horizon which is selected as three times the element size and α is taken to be 0.4 in this study. By default, the bond length should be less than the horizon, so the value of the influence function reduces with increasing bond length. The weighted volume m and dilatation ϑ of at a material point is calculated by

$$m < \boldsymbol{x} > = \int_{\Omega_x} \omega < \|\boldsymbol{\xi}\| > \|\boldsymbol{\xi}\|^2 \, \mathrm{d}V_{x'} \tag{5}$$

$$\vartheta < \boldsymbol{x} > = \frac{3}{m < \boldsymbol{x} >} \int_{\Omega_x} \omega < \|\boldsymbol{\xi}\| > \|\boldsymbol{\xi}\| \underline{e} \mathrm{d}V_{x'} \tag{6}$$

where $\underline{e} = \| \boldsymbol{Y} \| - \| \boldsymbol{\xi} \|$ represents the extension of a bond. It can be further divided into an isotropic part, $\underline{e}^{\mathrm{i}}$, and a deviatoric part $\underline{e}^{\mathrm{d}}$

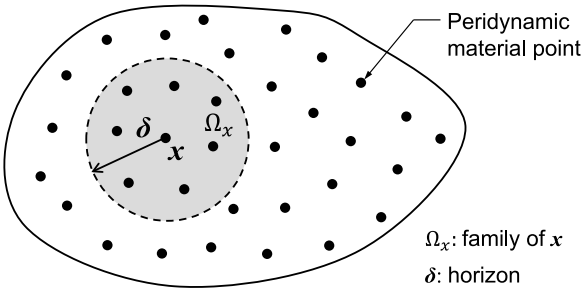

Fig. 1. Illustration of basic concepts in peridynamics.

where $\underline{e}^{\mathrm{i}} = \vartheta\langle \boldsymbol{x} \rangle \| \boldsymbol{\xi} \| /3$ and $\underline{e}^{\mathrm{d}} = \underline{e} - \underline{e}^{\mathrm{i}}$.

The ordinary SBPD is a pure peridynamic formulation of materials and does not involve engineering stress and strain terms. Inconveniences arise when complex material behaviours are to be modelled and when it is desirable to introduce classical constitutive models for their description. In addressing this issue, the non-ordinary SBPD theory [18] has been proposed to offer a framework for implementing material constitutive models based on engineering stress and strain relations. Material modelled with non-ordinary SBPD is often referred to as non-ordinary material. In the non-ordinary SBPD, the force state $\boldsymbol{T}$ is computed through

$$\boldsymbol{T} < \boldsymbol{x}' - \boldsymbol{x} >= \omega\langle \| \boldsymbol{\xi} \| \rangle \boldsymbol{P}_x \boldsymbol{K}_x^{-1} \boldsymbol{\xi} \tag{7}$$

where $\boldsymbol{P}_x$ represents the first Piola-Kirchhoff stress tensor and $\boldsymbol{K}_x$ is a non-local shape tensor. They are computed by

$$\boldsymbol{P}_x = \det(\boldsymbol{F}_x)\boldsymbol{\sigma}_x \boldsymbol{F}_x^{-1} \tag{8}$$

$$\boldsymbol{F}_x = \left[\int_{\Omega_x} \omega < \|\boldsymbol{\xi}\| > \boldsymbol{Y} \otimes \boldsymbol{\xi} \, \mathrm{d}V_{x'} \right] \boldsymbol{K}_x^{-1} \tag{9}$$

$$\boldsymbol{K}_x = \int_{\Omega_x} \omega < \|\boldsymbol{\xi}\| > \boldsymbol{\xi} \otimes \boldsymbol{\xi} \, \mathrm{d}V_{x'} \tag{10}$$

where $\boldsymbol{\sigma}_x$ refers to the Cauchy stress tensor and $\boldsymbol{F}_x$ is the non-local deformation gradient tensor. $\det(\boldsymbol{F}_x)$ calculates the determinant of $\boldsymbol{F}_x$. The symbol $\otimes$ denotes dyadic product between two vectors. The subscript refers to the point where the quantity is calculated. Classical constitutive material models can be conveniently implemented to compute the Cauchy stress based on the non-local deformation gradient, for assessing complex material behaviours. In this study, as we only address linear elastic solids, all solid materials are modelled as ordinary materials.

2.2. Bond breakage and material damage

The initiation and propagation of cracks are modelled by allowing the peridynamic bonds to break irreversibly. Once a bond is broken, the load originally borne on that bond is redistributed to neighbouring bonds and such process may trigger continuous breakage of peridynamic bonds which eventually simulates propagation of fractures. For elastic brittle materials that will be modelled in this study, a critical stretch damage model [42] is employed to simulate bond breakage. The model assumes that a bond breaks when its strain reaches a critical value. The critical bond strain can be related to the critical energy release rate of the material through

$$s_{\mathrm{c}} = \sqrt{\frac{5G_{\mathrm{c}}}{9K\delta}} \tag{11}$$

where G_{c} is a material constant representing the critical energy release rate. In the framework of peridynamics, damage of a material point can be expressed by a weighted percentage of broken bonds as

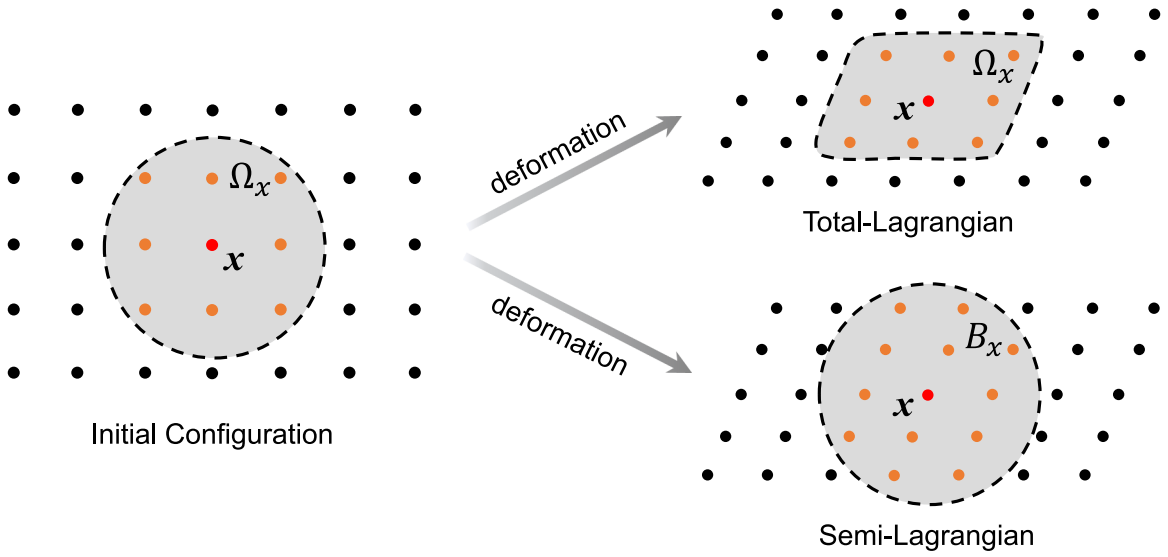

Fig. 2. Schematic illustration of the difference between total- and semi-Lagrangian formulations in peridynamics.

$$\varphi = 1 - \frac{\int_{\Omega_x} g < \boldsymbol{\xi} > \mathrm{d}V_{x'}}{\int_{\Omega_x} \mathrm{d}V_{x'}} \tag{12}$$

where $g\langle\boldsymbol{\xi}\rangle$ indicates the status of a bond. $g\langle\boldsymbol{\xi}\rangle$ equals 1 for all intact bonds and is set to zero for all broken bonds. Consequently, the damage φ equals zero for an intact material point and rises with increasing bond breakage to an upper limit of 1. The damage value can be used to locate fracture surfaces.

2.3. Semi-Lagrangian formulation

The classical PD theory is established on a total-Lagrangian formulation, such that the material response is calculated based on an initial, undeformed configuration. The formulation is naturally embedded with an assumption of small deformation and is not applicable for materials that undergo large deformation or for modelling fluid. The semi-Lagrangian formulation of PD has been developed as a remedy. With this formulation, the family of a material point maintains a constant shape regardless of the deformation. Consequently, the neighbours of a material point can continuously evolve with material deformation. This is illustrated in Fig. 2. It should be noted that the semi-Lagrangian formulation of PD is also referred to as Eulerian PD or updated Lagrangian particle hydrodynamics [32,35-36].

The semi-Lagrangian formulation of PD has been employed in the present work for modelling fluid. Its equation of motion writes

$$\rho_x \ddot{\boldsymbol{u}}_x = \int_{B_x} [\boldsymbol{T} < \boldsymbol{x}' - \boldsymbol{x} > - \boldsymbol{T} < \boldsymbol{x} - \boldsymbol{x}' >] \mathrm{d}V_{x'} + \boldsymbol{b}_x \tag{13}$$

which is in the same form of Eq. (1) except that the family of a material point $\boldsymbol{x}$, B_x, is being updated at each time step. To incorporate the constitutive relationship of fluids, the force state of semi-Lagrangian PD is calculated based on a non-ordinary SBPD form as

$$\boldsymbol{T} < \boldsymbol{x}' - \boldsymbol{x} > = \omega\langle \| \boldsymbol{Y} \| \rangle \boldsymbol{\sigma}_x \boldsymbol{M}_x^{-1} \boldsymbol{Y} \tag{14}$$

where the influence function ω is the same as shown in Eq. (4). The Gaussian form of influence function is known to offer good numerical stability [43]. For a fluid, the Cauchy stress $\boldsymbol{\sigma}_x$ is computed by

$$\boldsymbol{\sigma}_x = -p\boldsymbol{I} + 2\mu_s \dot{\epsilon} \tag{15}$$

where p is the fluid pressure, μ_s denotes the viscosity, and $\dot{\epsilon}$ is the shear strain rate tensor defined by

$$\dot{\epsilon} = \frac{1}{2}\left(\boldsymbol{L}_x + \boldsymbol{L}_x^T\right) - \frac{1}{3} L_{\mathrm{tr}} \boldsymbol{I} \tag{16}$$

$$\boldsymbol{L}_x = \left[\int_{B_x} \omega\langle \| \boldsymbol{Y} \| \rangle \dot{\boldsymbol{Y}} \otimes \boldsymbol{Y} \mathrm{d}V_{x'}\right] \boldsymbol{M}_x^{-1} \tag{17}$$

where $\boldsymbol{L}$ represents a non-local spatial velocity gradient tensor. The trace of $\boldsymbol{L}$, as denoted by L_{tr}, is the volumetric strain rate at a material point. L_{tr} is calculated at each time step to update material point volume. $\boldsymbol{M}_x$ represents the shape tensor corresponding to the current (deformed) configuration and is computed by

$$\boldsymbol{M}_x = \int_{B_x} \omega\langle \| \boldsymbol{Y} \| \rangle \boldsymbol{Y} \otimes \boldsymbol{Y} \mathrm{d}V_{x'} \tag{18}$$

Apparently, at each time step, the shape tensor of each material point needs to be updated. The semi-Lagrangian formulation is therefore computationally more expensive than the total-Lagrangian formulation.

It is worth mentioning that the semi-Lagrangian PD can be seen as a non-local approach for solving the Navier-Stokes (NS) equations in the form of

$$\frac{\mathrm{D}\rho}{\mathrm{D}t} + \rho \nabla \cdot \boldsymbol{v} = 0 \tag{19}$$

$$\rho \frac{\mathrm{D}\boldsymbol{v}}{\mathrm{D}t} = \nabla \cdot \boldsymbol{\sigma} + \boldsymbol{b} \tag{20}$$

where ρ and $\boldsymbol{v}$ represent density and velocity at a material point, respectively, and $\nabla\cdot$ denotes the spatial divergence operator. Key to solve the NS equations in the semi-Lagrangian PD is to approximate the spatial divergence by a non-local spatial differential operator [34] in the form of

$$\nabla \cdot (\boldsymbol{A}) \approx \int_{B_x} \omega\langle \parallel \boldsymbol{Y} \parallel \rangle \, \Delta \cdot (\boldsymbol{A}) \, \left[\boldsymbol{M}^{-1}\boldsymbol{Y}\right] \mathrm{d}V_{x'} \tag{21}$$

where $\boldsymbol{A}$ is an arbitrary vector field and $\Delta \cdot (\boldsymbol{A}) = \boldsymbol{A}^{x'} - \boldsymbol{A}^{x}$ is a finite difference operator. With the non-local spatial differential operator, the continuity equation and momentum equation of the NS equations are reformulated as

$$\frac{\mathrm{D}\rho}{\mathrm{D}t} = -\rho \int_{B_x} \omega\langle \parallel \boldsymbol{Y} \parallel \rangle \boldsymbol{v}\langle \boldsymbol{Y} \rangle \cdot \left(\boldsymbol{M}_x^{-1}\boldsymbol{Y}\right) \mathrm{d}V_{x'} \tag{22}$$

$$\rho \frac{\mathrm{D}\boldsymbol{v}}{\mathrm{D}t} = \int_{B_x} \omega\langle \parallel \boldsymbol{Y} \parallel \rangle \left(\boldsymbol{\sigma}_x \boldsymbol{M}_x^{-1} + \boldsymbol{\sigma}_{x'} \boldsymbol{M}_{x'}^{-1}\right) \boldsymbol{Y} \mathrm{d}V_{x'} + \boldsymbol{b}_x \tag{23}$$

Solving Eq. (22) is essentially equivalent to solving the volumetric strain using Eq. (17) and updating the volume and density at each material point. Eq. (23) is identical to the equation of motion in peridynamics. Therefore, the formulations presented in Eqs. (13) through (18) can be regarded as a reformulation of the NS equations for fluid in a non-local integral form.

The semi-Lagrangian formulation may experience pressure noise issue when simulating fluid, like what typically encountered in the SPH. To improve numerical stability, we apply a re-initialization of the fluid density field as following

$$\rho = \frac{\int_{B_x} \omega\langle \parallel \boldsymbol{Y} \parallel \rangle \, \mathrm{d}m_{x'}}{\int_{B_x} \omega\langle \parallel \boldsymbol{Y} \parallel \rangle \, \mathrm{d}V_{x'}} \tag{24}$$

where $m_{x'}$ and $V_{x'}$ represent the mass and volume of a neighbouring material point, respectively. This procedure is a smoothing of the density field using the neighbouring point information. The pressure field, which is calculated based on material density through an equation of state (EoS), is therefore smoothed by this procedure. In the present study, this procedure is implemented in the simulation of fluid injection at every two computational steps.

To enhance numerical stability, an artificial viscosity is often needed [32]. The artificial viscosity is represented by a force density term computed by

$$\boldsymbol{T}_{\mathrm{v}} = \frac{\upsilon^2}{\gamma\delta} \left(C_{\mathrm{q}} \rho_0 \phi^2 - C_{\mathrm{l}} \rho_0 c_0 \dot{\boldsymbol{Y}}\langle \boldsymbol{Y} \rangle \cdot \boldsymbol{N}\langle \boldsymbol{Y} \rangle\right) \boldsymbol{N}\langle \boldsymbol{Y} \rangle \tag{25}$$

which consists of a linear term and a quadratic term with two coefficients C_{l} and C_{q}, respectively. Parameter ρ_0 and c_0 refer to the reference (initial) density of the material and bulk wave speed, respectively. $\boldsymbol{N}\langle \boldsymbol{Y} \rangle$ denotes the unit vector of the deformed bond. γ is an average volume calculated by

$$\gamma = \int_{\Omega_x} \omega\langle \parallel \boldsymbol{Y} \parallel \rangle \, \mathrm{d}V_{x'} \tag{26}$$

and υ represents relative volume, calculated by the ratio of initial and current density at the material point:

$$\upsilon = \frac{\rho_0}{\rho} \tag{27}$$

The current density can be obtained based on the volumetric strain at the point. Lastly, the effective velocity change within the *family*, as denoted by ϕ, is calculated by

$$\phi = \frac{1}{\gamma} \int_{B_x} \omega\langle \parallel \boldsymbol{Y} \parallel \rangle \dot{\boldsymbol{Y}}\langle \boldsymbol{Y} \rangle \cdot \boldsymbol{N}\langle \boldsymbol{Y} \rangle \mathrm{d}V_{x'} \tag{28}$$

The artificial viscosity serves the same purpose as the viscous dissipative pressure term commonly added in SPH simulations [44]. It is added into the right side of the equation of motion of PD. The artificial viscosity in Eqs. (25) to (28) can also be applied in total-Lagrangian formulations by using the bond vector at the reference configuration rather than the deformed configuration.

In particle-based methods, clustering of particles is a commonly known issue which hinders the numerical stability for long-duration simulations. In the case of SPH, particle clustering can result from both tensile instability and the choice of kernel function [45]. In the present study, to address the similar issue in semi-Lagrangian PD, a point shifting technique is introduced based on the method proposed by Xu et al. [45] in SPH, which adjusts the position vector of each material point by adding an artificial displacement $\Delta \boldsymbol{x}_i$ and interpolates hydrodynamic variables at the new position based on first-order Taylor series. The modification term at each step can be expressed as

$$\Delta \boldsymbol{x}_i = C_{\mathrm{PST}} v_{\max} \mathrm{d}t \sum_{j=1}^{N_i} \frac{\left(\frac{1}{N_i} \sum_{j=1}^{N_i} \| \boldsymbol{Y} \| \right)^2}{\| \boldsymbol{Y} \|^2} \boldsymbol{N} \langle \boldsymbol{Y} \rangle. \tag{29}$$

where C_{PST} is a shifting coefficient, which directly determines the shifting distance. The shifting distance should be large enough to effectively prevent particle clustering and small enough not to cause numerical errors due to the Taylor series correction. It has been shown by test cases in Xu et al. [45] that values of C_{PST} within the range of 0.01–0.1 meet the criteria mentioned above. However, one should determine specific value of C_{PST} carefully based on the model size and deformation of fluid phase. Zero or a too small C_{PST} cannot prevent particle clustering effectively and consequently the simulation terminates before expected due to zero bond length or infinite force. On the contrary, a too large C_{PST} result in an excessive distance between particles which clearly deviates from the actual condition. $v_{\max}$ represents the maximum expected velocity of fluid material points throughout the computational domain. For instance, in the case of a dam break problem, $v_{\max}$ may be estimated as $\sqrt{2gH}$, where H is the height of water column; in the case of hydraulic fracturing or jetting problem, $v_{\max}$ may be adopted as the velocity of injected or jetted fluid. $\mathrm{d}t$ is the time step. N_i denotes the number of neighbouring points for material point $\boldsymbol{x}_i$.

3. Fluid-Solid interactions

A key part in simulating fluid-driven fractures is the modelling of the interactions between solid and fluid material points. When both solid and fluid are simulated within the PD framework, FSI can be conveniently modelled by coupling the total- and semi-Lagrangian formulations of PD. At the interface, we assume that the solid material points to be fictitious fluid material points when they are located within the horizon of a fluid material point. This is illustrated in Fig. 3. The fictitious fluid material points are treated as a normal neighbouring point of the real fluid material point when calculating the shape tensor and spatial velocity gradient tensor in Eqs. (17) and (18). For any bond that crosses the solid-fluid interface, the bond force density is calculated by

$$\boldsymbol{T}_{\mathrm{FSI}} = \boldsymbol{T}_{\mathrm{f}} + \boldsymbol{T}_r \tag{30}$$

where $\boldsymbol{T}_{\mathrm{f}}$ is the interaction force calculated following the semi-Lagrangian PD theory

$$\boldsymbol{T}_{\mathrm{f}} = \omega \langle \| \boldsymbol{Y} \| \rangle \boldsymbol{\sigma}_x \boldsymbol{M}_x^{-1} \boldsymbol{Y} \ (x \in B_s) \tag{31}$$

In this calculation, $\boldsymbol{x}$ is a real fluid material point and B_s denotes the set of neighbouring points which are fictitious fluid material points. The shape tensor of a fluid material point at the interface is calculated by

$$\boldsymbol{M}_x = \int_{x' \notin B_s} \omega \langle \| \boldsymbol{Y} \| \rangle \boldsymbol{Y} \otimes \boldsymbol{Y} \mathrm{d}V_{x'} + \int_{x' \in B_s} \omega \langle \| \boldsymbol{Y} \| \rangle (1 - \varphi_{x'}) \boldsymbol{Y} \otimes \boldsymbol{Y} \mathrm{d}V_{x'} \tag{32}$$

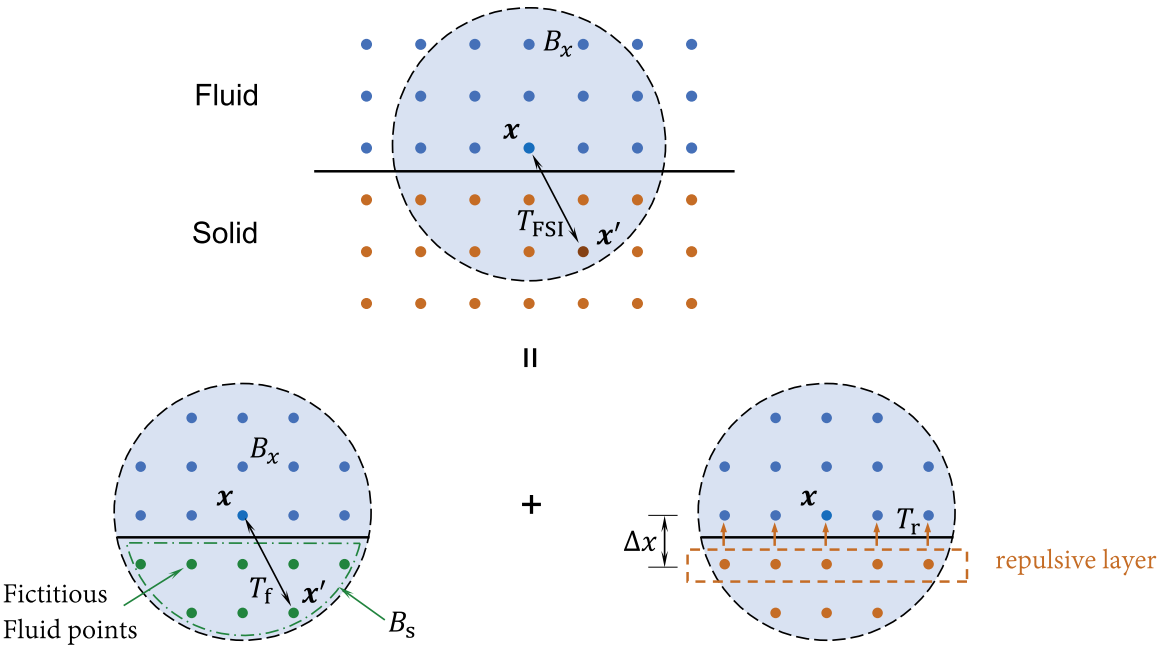

Fig. 3. Schematic illustration of the concepts and quantities in modelling fluid-solid interactions.

where $\varphi_{x'}$ represents the damage at a neighbouring solid material point that is treated as a fictitious fluid material point. The coefficient $(1-\varphi_{x'})$ is utilized here to enable fluid infiltration into damaged solids.

However, it is worth noting that enabling fluid infiltration into damaged solids does not imply penetration of fluids into intact solids, for example, the unphysical phenomenon that fluid material points penetrate the rigid wall in a dam break simulation. In the present study, we assume an idealized condition that the fluid material points cannot permeate into intact solid. Implementing only Eq. (31) cannot guarantee such non-penetration condition. An additional repulsive bond force density term $\boldsymbol{T}_{\mathrm{r}}$ is applied at a portion of the interface bonds to prevent interpenetration of material points at the interface. The definition is similar to [46] which was originally used for modelling fluid-solid interactions with SPH method. The term $\boldsymbol{T}_{\mathrm{r}}$ writes

$$\boldsymbol{T}_{\mathrm{r}} = -C_{\mathrm{RF}} c_0^2 f(\eta)\left(1-\frac{\| \boldsymbol{Y} \|}{\Delta x}\right)\frac{\boldsymbol{Y}}{\| \boldsymbol{Y} \|^2} \tag{33}$$

where C_{RF} is a coefficient that controls the magnitude of repulsive force. The basic criterion of determining C_{RF} is that it should be large enough to prevent unphysical penetration effectively and small enough to have minimal effect on fluid motion and computational accuracy. Its value should be calibrated and validated against experimental or reference data to ensure the accuracy and reliability of the simulation results. According to our tests and the reference [46], a value of 0.01 for C_{RF} generally satisfies the criterion mentioned above. η is a parameter related to bond length and horizon and can be calculated by $\| \boldsymbol{Y} \| / 0.75\delta$. $f(\eta)$ is defined in the form of B-spline kernel function as [47]

$$f(\eta) = \begin{cases} \frac{2}{3}, & 0 < \eta \le \frac{2}{3} \\ 2\eta - 1.5\eta^2, & \frac{2}{3} < \eta \le 1 \\ 0.5(2-\eta)^2, & 1 < \eta \le 2 \\ 0, & \text{otherwise} \end{cases} \tag{34}$$

and Δx represents the size of solid material point (cubic root of the volume in 3D, or square root of area in 2D). This repulsive force term is applied between fluid material points adjacent to the interface and solid materials points that are immediate neighbours of those fluid material points, as illustrated in Fig. 3. This algorithm is intended to have minimal effect on fluid motion and computational accuracy while effectively prevents unphysical penetration. Taking a smaller or zero C_{RF} may allow the fluid material points to seep into the intact solid material domain. This naturally simulates fluid seepage or penetration into the solid and may better suit scenarios where the solid material is porous or with high permeability. Nonetheless, the robustness, stability, and accuracy of the formulation in those scenarios require careful examination and will be addressed in a separate study.

Implementation of the above FSI formulation can be embedded in the computation of fluid. Velocity and pressure constraints can also be applied on the fictitious solid points to model free-slip or no-slip boundary conditions. Formulation for the solid material will not be affected by the FSI. In other words, the solid material can be modelled with either state-based (ordinary or non-ordinary) or bond-based PD formulation. The presented FSI model thus offers high versatility to the coupled computational framework. Nonetheless, selection of the FSI model is at the discretion of the modeller and should be based on the specific case to be simulated. Many other FSI models can be found in the literature for a variety of FSI scenarios, such as the two-way interaction technique where fictitious points are modelled in both solid and fluid domains [30].

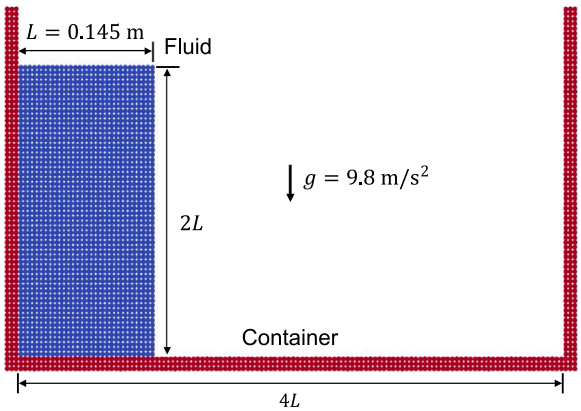

Fig. 4. PD discretization of 2D Dam break model.

4. Numerical simulations

In this section, we first simulate two-dimensional (2D) and three-dimensional (3D) dam break problems to validate both the semi-Lagrangian PD fluid model and the coupled FSI algorithm. The simulation results are compared with laboratory experiments. Subsequently, we extend the coupled computational framework to simulate two classical problems, one for crack deformation under hydrostatic water pressures and the other for fluid injection induced fracturing. Analytical solutions are available for both problems and are used for validation. Furthermore, we conduct simulations on an actual hydraulic fracturing in sandstone to demonstrate the capability of the proposed method with results compared with experimental data.

4.1. Dam break simulations

To demonstrate the efficacy of the proposed method in modelling fluid with FSI, we first present a benchmark of the classical dam break problem, considering both 2D and 3D conditions. The 2D dam break model is illustrated in Fig. 4. The flow is driven by gravity of 9.8 m/s^2. The flow is confined within a rigid container with an upper opening. The water column has a width of 0.145 m and a height of 0.29 m. The material point size is set at 5 mm for both fluid and the rigid container, and the entire fluid domain is discretized with 1682 material points. In the 2D simulation presented herein, the material point size refers to the dimension of a square whose area is the same as that represented by a material point. The simulation is found insensitive to the material point size when it is smaller than 5 mm. The horizon of the fluid and the thickness of the container are both set at three times the material point size.

To describe the relation between pressure and density of fluid, the equation of state proposed by Monaghan [44] is employed here as

$$p = \frac{\rho c_0^2}{n}\left(\frac{1}{\upsilon^n} - 1\right) + p_b \tag{35}$$

where n is one fitting parameter, which can be determined based on test data. p_b is a background pressure. υ is relative volume defined in Eq. (27). In current simulation, the fluid is assumed to be water, with the parameters n set to 7.0 [48]. The container is assumed to be made of steel. The parameters of both the fluid and the container are summarized in Table 1. It is noteworthy that, in contrast to many previous particle-based methods [39-40,49] which typically model the solid using mirroring particles or fictitious particles that serve solely as boundary conditions, the proposed method herein models both the fluid and the container using actual PD material points.

The configuration of the simulation follows an experiment as presented in [50] for the convenience of comparison. A comparison of the simulated fluid profile with experiment at different time is shown in Fig. 5. As driven by the gravity force, the water column collapses gradually and hit the right boundary of container at about 0.25 s, with water bounced back afterwards. The simulation results are found to match well with the experimental results throughout the modelling time. A further quantitative comparison is carried out with respect to the front of the collapsing water as exhibited in Fig. 6. The experimental data given by Koshizuka [51] and Martin et al. [52] are included for comparison. A reasonable match between the numerical and experimental data can be seen. In the simulation, no unphysical penetration of fluid material points into solid domain has been observed. It is also worth noting that the material point distribution of the proposed method is rather uniform throughout the simulation (i.e., point clustering is largely eliminated) and there are no notable voids between the container and the fluid. This demonstrates the merits of the proposed method in simulating fluid and FSI.

A 3D dam break problem is further simulated for benchmarking. A cross section of the model is schematically shown in Fig. 7. In the model, an obstacle perpendicular to the flow path is set on the way. All parameters adopted in this simulation are the same as those used in the 2D problem, except for the material point size which is set larger to 6 mm for better computational efficiency. The total number of material points is 27,648 for the fluid and 51,528 for the solid container (including the obstacle). The simulated profile of the collapsing water is shown in Fig. 8 at different times with comparison to experiment conducted by Koshizuka [51]. Again, good agreement can be found with respect to the advancement of the collapsing water. The interactions between fluid and the obstacle are well captured. The capability of the proposed method in simulating fluid and FSI problems is therefore demonstrated in both 2D and 3D dam break problems.

4.2. Crack profile under hydrostatic pressure

A benchmark model is developed to test the performance of the proposed computational framework in simulating solid deformation under hydrostatic pressure. The model simulates the profile of a static crack in elastic solid pressurized by fluid. The analytical solution for the fracture aperture profile in a 2D infinite elastic domain is given by [53] in the form of

Table 1
Parameters for dam break simulation.

Parameters	Fluid	Container
Density: kg/m^3	998	8000
Bulk modulus: GPa	2.2	160
Poisson's ratio	/	0.3
$C_{PST} = 0.01$, $C_{RF} = 0.01$, $v_{max} = 2.38$ m/s, $c_0 = 1500$ m/s, $n = 7.0$, $\delta = 3\Delta x$.		

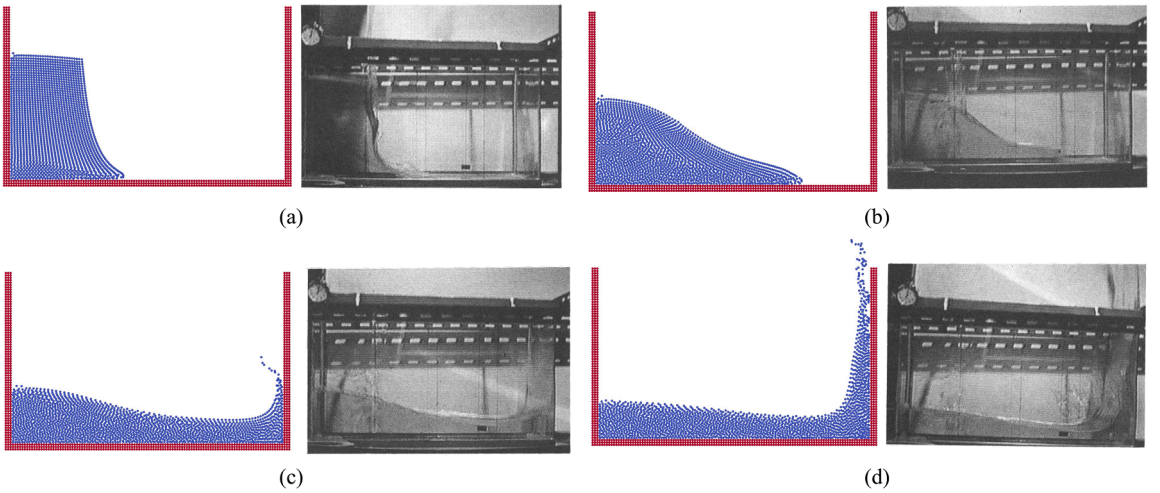

Fig. 5. Comparisons of fluid contour between experiment [51] and simulation for: (a) $t = 0.1$ s; (b) $t = 0.2$ s; (c) $t = 0.3$ s; and (d) $t = 0.4$ s.

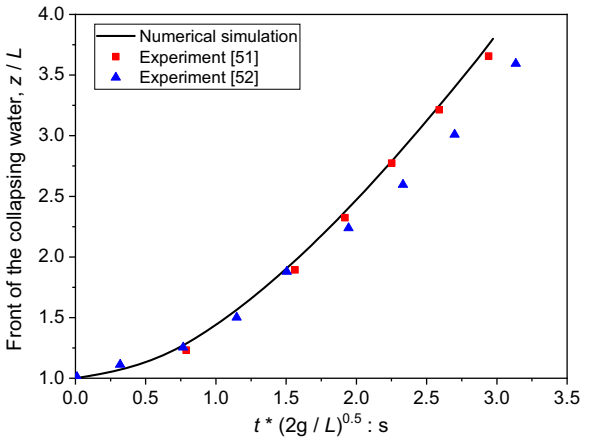

Fig. 6. Position of the front of collapsing water with normalized time.

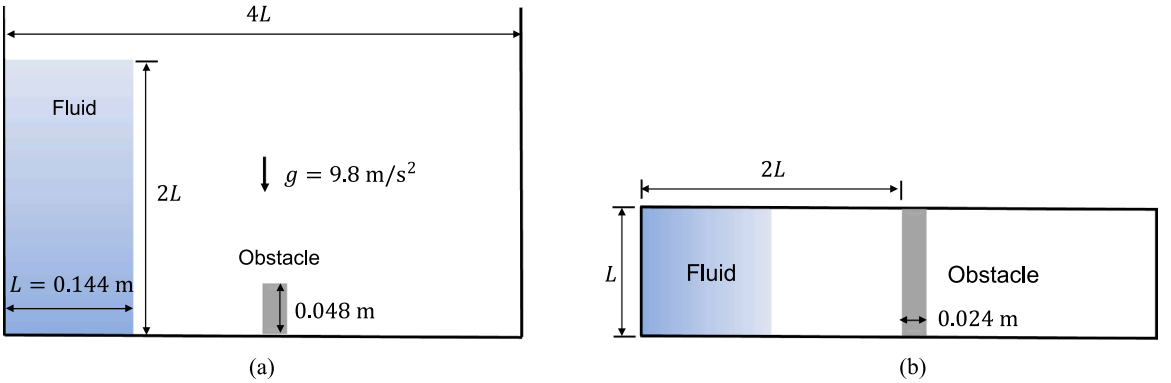

Fig. 7. Configuration of the 3D dam break model: (a) front view; and (b) top view.

$$w = \frac{4pl}{E}\sqrt{1-\left(\frac{x}{l}\right)^2} \tag{36}$$

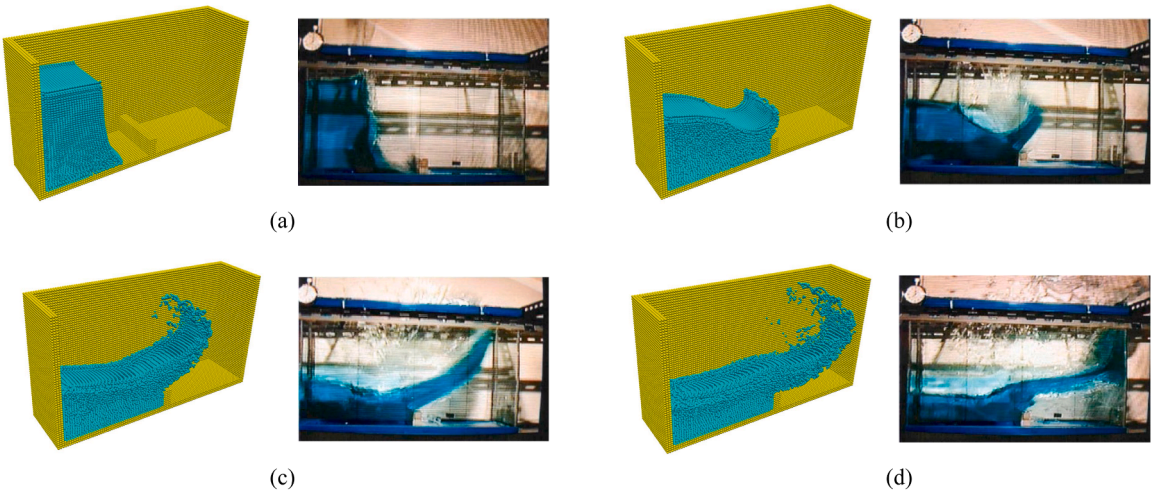

Fig. 8. Comparisons of fluid contour between experiment [51] and simulation for: (a) $t = 0.1$ s; (b) $t = 0.2$ s; (c) $t = 0.3$ s; and (d) $t = 0.4$ s.

where p is the fluid pressure; l represents half-length of the crack; x denotes the position along the crack; and $E' = E/(1-\nu^2)$ denotes the plane strain modulus where E and ν are the Young's modulus and Poisson's ratio, respectively. The numerical model considers a quarter of the domain as shown in Fig. 9 with a size of 10.0 m $\times$ 10.0 m. The half-length of the crack is taken to be 1.0 m. Considering the symmetrical features of the problem, we fix the deformation of material points on the $y = 0$ edge (beyond the crack) and the $x = 0$ edge along the y and x direction, respectively, as a boundary condition. Ordinary SBPD is known to have surface effect owning to the reduced number of neighbours near material boundaries. To enhance the computation accuracy at the boundaries, we model a layer of fictitious points with thickness of a horizon along the two boundaries and the above-described boundary conditions are also assigned to those fictitious points. The properties of both fluid and solid materials in the simulation are given in Table 2. Fluid material points are modelled in a rectangular region adjacent to the crack and are compressed to generate hydrostatic pressure. The fluid pressure is applied on the crack through the FSI model presented in Section 3. The modelled fluid domain is extended beyond the $x = 0$ edge for a distance of a horizon to mitigate the boundary effect at the fluid-solid interface.

We first select an element size of 0.025 m for both fluid and solid to perform two simulations with different fluid pressures. The obtained crack aperture profiles are compared with analytical solutions in Fig. 10 where good agreement is observed. The calculated aperture is generally within 1% of the analytical solution. The results confirm the capacity of the non-local peridynamics approach and the FSI algorithm in giving correct prediction of deformation in solid under hydrostatic pressure.

In Fig. 11 we further investigate the accuracy and convergence of the solution with five different element sizes ranging from 0.0125 m (1/80 the crack length) to 0.2 m (1/5 the crack length) under different hydrostatic pressures. The error of the numerical solution is

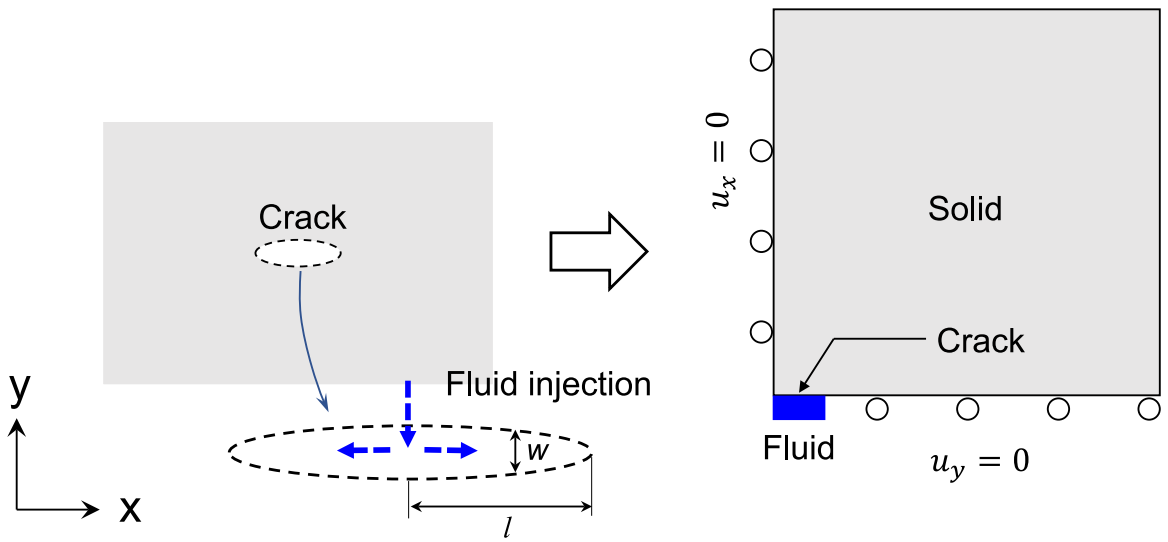

Fig. 9. Schematic illustration of the crack profile benchmark model.

Table 2
Parameters for simulation of crack profile under hydrostatic pressure.

Parameters	Fluid	Solid
Density: kg/m^3	998	2500
Bulk modulus: GPa	2.2	/
Young's modulus: GPa	/	10
Poisson's ratio	/	0.2
$C_{\mathrm{PST}} = 0.0$, $C_{\mathrm{RF}} = 0.01$, $c_0 = 1500$ m/s; $n = 7.0$, $\delta = 3\Delta x$.		

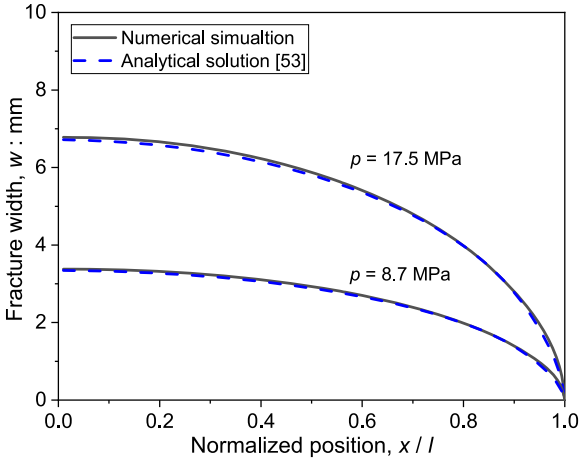

Fig. 10. Comparison of crack aperture profile from simulation and analytical solution.

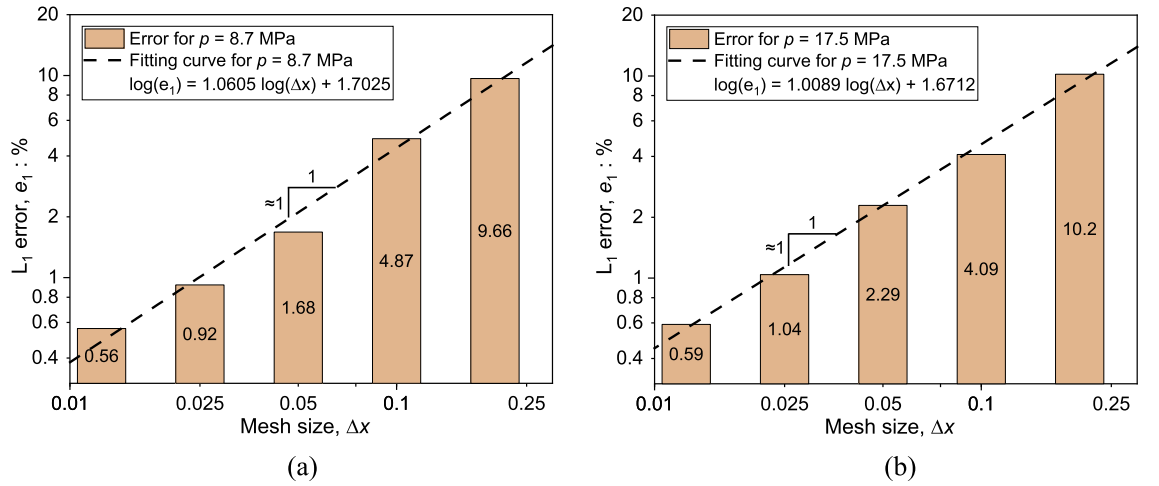

Fig. 11. Variation of L_1 error with element size for: (a) $p = 17.5$ MPa; and (b) $p = 8.7$ MPa.

indicated by the relative L_1 loss which is calculated by $e_1 = \sum_{n=1}^{N}(w_{\mathrm{a}} - w_{\mathrm{n}})/(w_{\mathrm{a}}N)$, where w_{a} and w_{n} represent analytical and numerical solution of the crack aperture at a point, respectively. A total of nine points ($N = 9$) are selected along the crack direction with a uniform interval. The calculated L_1 error is found to reduce with element size monotonically. It can be seen that even with a rather coarse discretization (e.g., $\Delta x = 0.2$ m) the numerical solution does not deviate notably from the analytical solution with the L_1 error at about 10%. With finer discretization, the L_1 error drops by one order and offers good computational accuracy. The convergence slope for the two cases in L_1 error exhibits first order accuracy. Therefore, as the mesh size approaches zero, the nonlocal method approaches the exact solution at a rate of Δx. The presented simulation confirms the capacity of the proposed computational framework in modelling deformation at cracks with pressurized fluid.

4.3. KGD hydraulic fracturing model

The KGD fracturing model is one of the most classical analytical models for hydraulic fracturing introduced by Geertsma and Klerk [54]. It deals with the propagation of a linearly expanding plane strain fracture in an impermeable elastic solid, as schematically illustrated in Fig. 12(a). The analytical solution is based on the theory of elasticity which describes the deformation of solid, the linear elastic fracture mechanics which governs the propagation of the fracture, and a lubrication equation which describes the flow in the fracture. The growth of the fracture can be classified into toughness-dominated and viscosity-dominated regimes based on the mechanism of energy consumption. The toughness-dominated regime is represented by negligible energy dissipation in viscous fluid flow compared to the energy on fracturing solid whereas the viscosity-dominated regime involves significant energy dissipation in overcoming the viscosity of fluid. When a low-viscosity Newtonian fluid, such as water, is injected into the formation, the KGD fracture may be purely toughness-dominated without a transition from the viscosity-dominated region to the toughness-dominated region [55]. The present study deals with the toughness-dominated fractures only. The analytical solutions of the length of facture and injection pressure developed at the injection point are derived by [55] as

$$L = \frac{2}{\pi^{\frac{2}{5}}}\left(\frac{E^{'}qt}{K^{'}}\right)^{\frac{2}{3}} \tag{37}$$

$$p = \frac{\pi^{\frac{1}{5}}}{8}\left(\frac{K^{'4}}{E^{'}qt}\right)^{\frac{1}{3}} \tag{38}$$

in which q is the flow rate; t is the injection time; $E^{'}$ is the plane strain modulus; and $K^{'}$ can be further expressed as

$$K^{'} = 4\sqrt{\frac{2}{\pi}}K_{\mathrm{IC}} \tag{39}$$

where K_{IC} represents the mode-I fracture toughness.

A 2D plane strain hydraulic fracturing model is set up as illustrated in Fig. 12(b) for which the simulation results are compared with the KGD analytical model. The solid specimen has a dimension of 200 mm × 150 mm. The solid material is assumed to be a typical brittle material [56] with properties given in Table 3. The solid material is confined by a 1 MPa compressive stress in x-direction and the upper boundary is fixed in y-direction to avoid rigid movement induced by fluid injection. Water is injected into the solid through a tube located at the top. An initial crack with a length of 10 mm and a width of 4 mm is assumed to be located at the upper middle of the solid. The tube is simulated by two strips of solid material points, each has a thickness three times of the element size of the material point. The tube is assumed to be fixed and has the same properties as the solids. The element size of all materials is taken to be 1 mm. The injection speed of water is set to be 0.2 m/s, corresponding to an injection rate of 0.0008 m^3/s. The total simulation time is 0.1 s with time step taken as 5.0×10^{-7} s.

Presented in Fig. 13 are the initiation and propagation process of fracture as well as the movement of fluid. The totally damaged ($\varphi = 1$) solid material points are deleted for clarification. The fracture initiates quickly at the first a few thousand steps. At about 5 ms, the fluid is seen squeezed into the fracture. The fluid drives the growth of the fracture by exerting forces perpendicular to the fracture surface as illustrated in Fig. 14. The forces being applied on the solid material near the fluid-solid interface tend to open the crack and the extent of such forces grow with the continued infiltration of fluid. The fracture induced by fluid injection is found to be approximately a straight line, which is the same as the analytical solution. It is noted that the fracture does not evolve perfectly

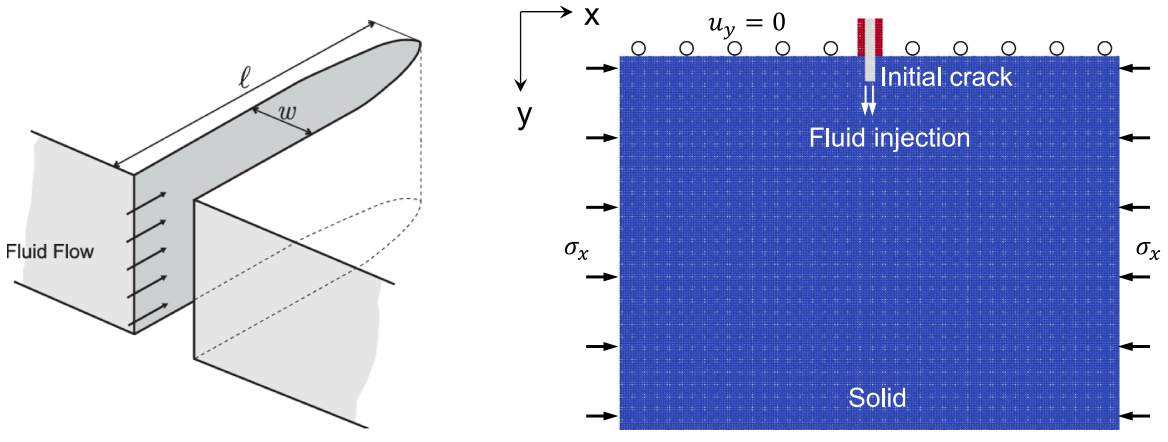

Fig. 12. Schematic illustration of: (a) KGD analytical model [16]; and (b) numerical model.

Table 3
Parameters for KGD hydraulic fracturing simulation.

Parameters	Fluid	Solid & Tube
Density: kg/m^3	998	1180
Bulk modulus: GPa	2.2	/
Young's modulus: GPa	/	2.8
Poisson's ratio	/	0.37
Fracture toughness: MPa·m$^{0.5}$	/	1.88
$C_{\mathrm{PST}} = 0.01$, $C_{\mathrm{RF}} = 0.01$, $v_{\max} = 0.2$ m/s, $c_0 = 1500$ m/s, $n = 7.0$, $\delta = 3\Delta x$.		

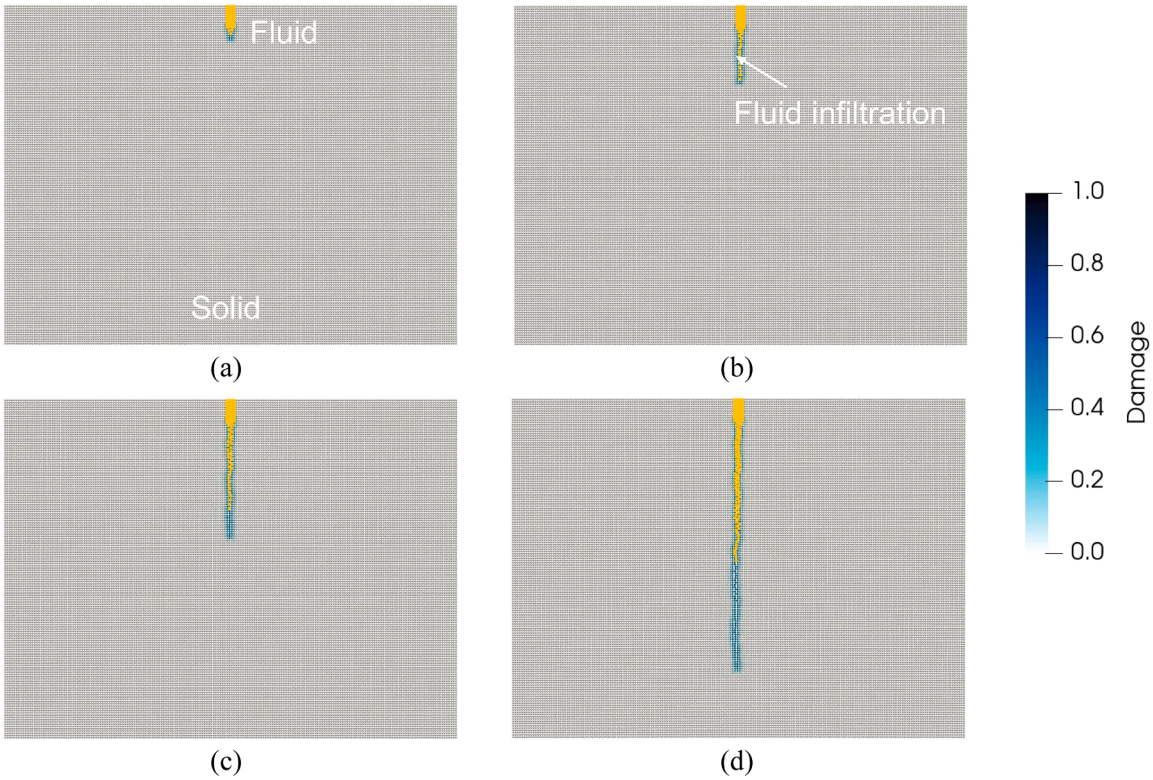

Fig. 13. Progress of fractures in solid and fluid infiltration into fractures obtained from simulation at: (a) 5 ms; (b) 25 ms; (c) 50 ms and (d) 100 ms.

vertically which is likely due to the non-locality of PD and the semi-Lagrangian formulation which tend to amplify or accumulate even slight numerical perturbations. With the progress of the fracture, it is observed that the fluid pressure gradually reduces and consequently the force density at the FSI decreases. The observed fluid injection pressure (i.e., the fluid pressure at the top of the initial crack) from the simulation is plotted together with the analytical solution in Fig. 15(a), which shows a general agreement. At the beginning of the simulation, the pressure in the fluid starts to build up with the injection process. The first peak in the pressure curve indicates the start of crack propagation. The injection pressure drops dramatically after the peak due to the opening created by fracturing. The injection pressure builds up again as fluid filling the voids of the fracture, and it gradually drops with further steady growth of the fracture. The analytical solution for the toughness-dominated regime assumes that the fracture is fully filled by fluid at all times. Therefore, the result is only presented by a monotonic decreasing curve and the transient phenomena is not reflected. Some fluctuations in the simulation result are observed and it is expected to be a result of disturbance due to bond breakage (i.e., fracture extension) on fluid field. It is expected that the fluctuations can be further minimized with finer meshing for both fluid and solid.

The comparison of the length of fracture between the simulation and analytical solution is shown in Fig. 15(b). The length of fracture in the simulation is measured along the y-axis based on the fracture front, which is denoted by the furthest point having a damage not less than 0.4. It can be found that the numerical solution generally matches the analytical solution with similar trend. Note that the actual fracture is not perfectly straight in the simulation and as such, it is not surprising to observe some discrepancies between the simulation result and analytical solution. The fracture appears to be readily filled with fluid in the initial stage of injection as shown in Fig. 13. At about halfway during the simulation, the fracture front and fluid front begin to deviate, forming a fluid lag [57–59]. Formation of the fluid lag is known to be associated with fluid viscosity, injection rate, permeability of rock and many other properties. In the numerical simulation, the phenomenon can also be partially attributed to the fact that the material point size of fluid is relatively

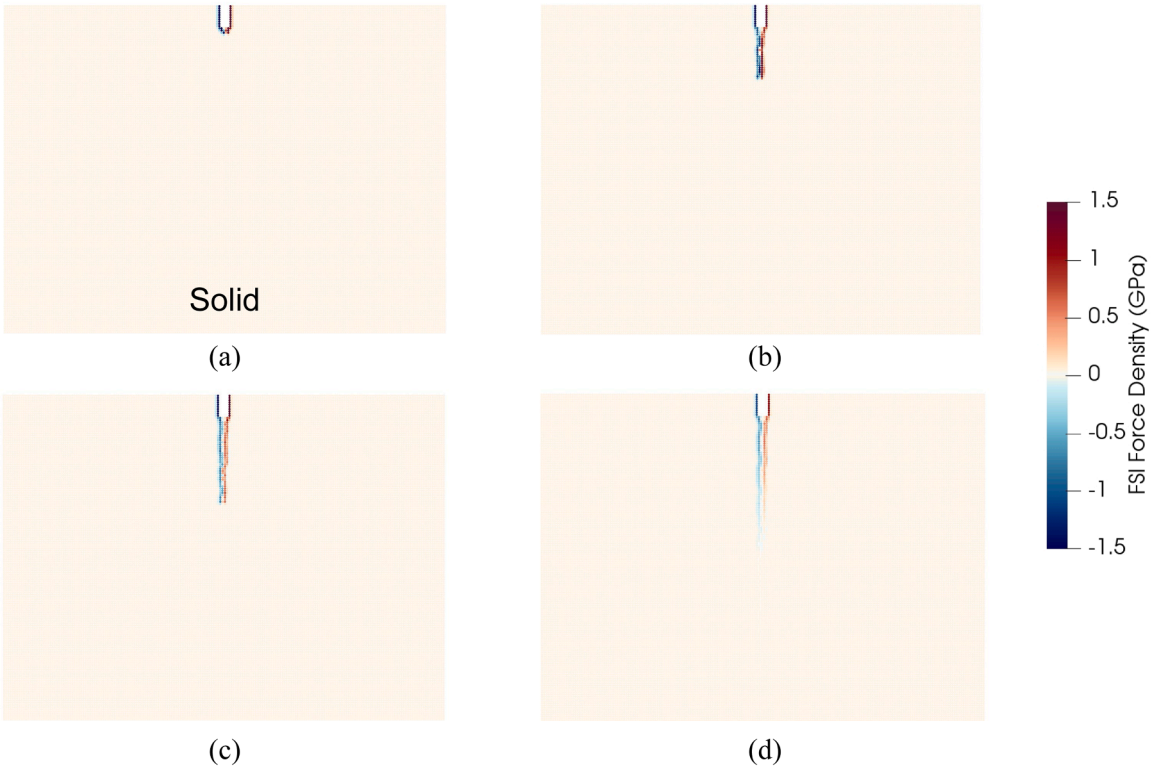

Fig. 14. FSI force density in horizontal direction at: (a) 5 ms; (b) 25 ms; (c) 50 ms; and (d) 100 ms.

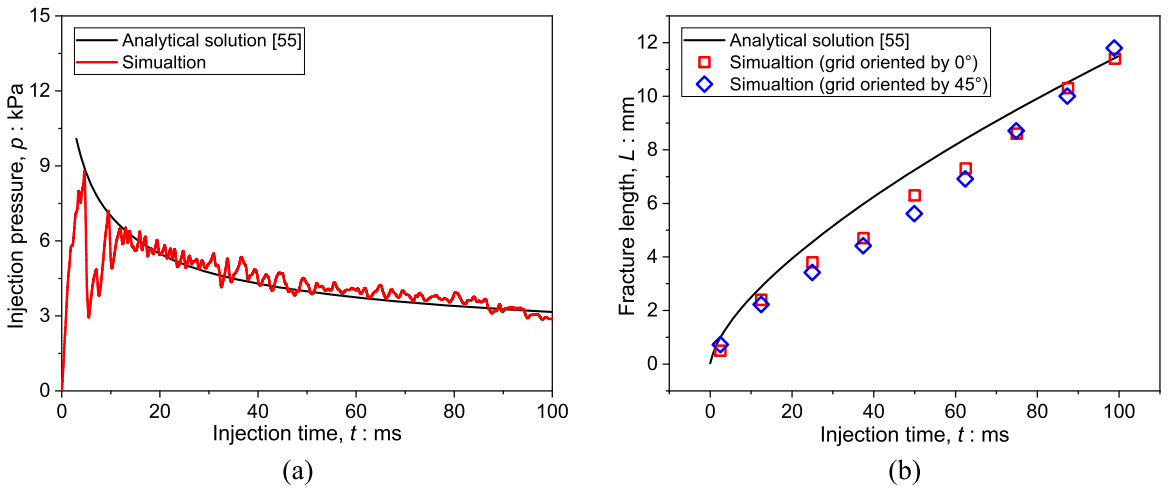

Fig. 15. Comparison of: (a) injection pressure developed at injection point; and (b) fracture length between numerical and analytical solutions.

large compared to the fracture width so that the fluid material points cannot easily enter the fracture. Using a smaller material points size is expected to improve the situation. Nonetheless, excessively small material point size would induce unaffordable computational costs. The dual-horizon theory [60] may be potentially useful if different material point sizes are to be used for fluid and solid. It is nonetheless out of the scope of the present study and may worth investigation in the future.

In Fig. 15(b) we further extend our study to examine the sensitivity of simulation results on the material point discretization pattern. In the previous simulation, the material points were generated with a square grid in both horizontal and vertical directions. The grid is now rotated by 45° and all material points are regenerated for analysis. It has been confirmed that the propagation develops along the vertical direction. The propagation speed of the fracture, as shown in the figure, is insensitive to the discretization pattern with the adopted material point size ($\Delta x = 1$ mm). As discussed in Section 4.2, the proposed method exhibits convergence as the

element size decreases. Consequently, with a fine mesh utilized in the KGD analysis, the associated error should be negligible irrespective of the spatial discretization pattern.

4.4. Injection-induced brittle fracture in sandstone

In this example, we simulate a typical laboratory scale hydraulic fracture test where fluid is injected into a sandstone specimen to trigger fractures [61]. The sandstone specimen is cylindrical with a height of 140 mm and a radius of 50 mm. The fluid is injected through a steel tube inserted in a borehole drilled at the centre of the specimen at a constant rate of 10 ml/min. The borehole has a diameter of 6.35 mm. The numerical model is set up as shown in Fig. 16(a). The sandstone, the tube, and the fluid are discretized with an element size of 1.5 mm, 1.33 mm and 1.0 mm, respectively, leading to a total number of 342,774 material points. The tube is modelled with an inner radius of 5 mm and an outer radius of 9 mm placed immediately inside the borehole. The borehole is 20 mm longer than the tube where the sandstone is exposed to the injection fluid. The specimen is confined in the experiment by an initial vertical stress of 10.3 MPa, and a horizontal stress of 20.7 MPa and 3.45 MPa along the two perpendicular directions, respectively. Since traction boundary conditions cannot be directly applied in PD, the initial stress is implemented as a body force on three layers of material points on the outer boundary near the maximum and minimum coordinates along the x and y directions. The body force is linearly increased during the first 400 simulation steps to the target level. The bottom three layers of the sandstone has been assigned with a fixed boundary condition along the vertical direction. The tube is fixed in the simulation and the interaction between the tube and sandstone is modelled with a short-range force contact model as detailed in [62].

The properties of three materials are summarized in Table 4 based on [63–64] for sandstone and [61,65] for vegetable oil. The injection fluid is modelled following the semi-Lagrangian PD formulation in conjunction with the equation of state where the fitting parameters n taken to be 4.0 as interpreted from the compression test in [65]. The injection process is simulated by letting all fluid material points above the bottom of the tube to move at a constant vertical velocity of 1 m/s towards the interior of the sandstone. Injection starts after the confining stress has been applied. The rate of injection in numerical model is selected larger than that in experiment for the sake of computational efficiency. To stabilize the simulation and mitigate the dynamic effect, an artificial viscosity has been applied to the fluid with coefficients C_l and C_q both taken to be 0.5. A damping coefficient of 0.01 is applied to tamper the dynamic effect. The time step in the simulation is selected to be 2.5×10^{-7} s with a total number of 8000 simulation steps. The computation takes about 1.5 hrs running on 24 Intel® i9–12,900 CPUs at 3.0 GHz.

The simulation results are presented in Fig. 16 for both fluid pressure and the damage in solid. The pressure of fluid below the tube is of interest in this study since this pressure triggers the fracture in the sandstone. The fluid pressure within the tube does not have particular significance as the fluid is subject to the constant velocity condition and does not interact with the sandstone. An interior view of the evolving fracture surfaces is shown in Fig. 17. As expected, the fluid pressure beneath the tube gradually accumulates with the progress of injection, and the fracture is found to initiate near the borehole along the radial direction as shown in Fig. 16(b) and Fig. 17(a). Further injection does not lead to a subsequent increase in fluid pressure due the opening created by the fracture. The fluid pressure decreases drastically while the fractures propagate, as shown in Fig. 16(c)-(d). The fracture is observed to propagate primarily along the radial direction until it reaches the edge of the specimen. With continued injection, vertical crack can also be seen below the borehole as shown in Fig. 17(c). At the end of the simulation, the fracture surface is almost planar and is situated parallel to the maximum principal stress direction. The obtained fracture surface agrees reasonably well with the recorded acoustic emission events in experiment as shown in Fig. 17(d)-(e).

Presented in Fig. 18 is the evolution of fluid pressure during the injection process. The time after injection is normalized by t_{m} which represents the time when the maximum injection pressure is reached. The evolution of pressure is found agree with experimental records before the peak. The injection pressure reaches its peak near 18 MPa and drops drastically since then. The pressure drop is slower in our simulation probably due to the applied artificial viscosity and fast injection. The post-peak pressure evolution does not completely fit with the experimental records due to many other factors that cannot be faithfully captured in the simulation, such as the existence of pores and fluid permeation into intact solids which are not explicitly modelled. However, the simulation results accurately capture the peak pressure and reflect the overall evolution trend of the fluid pressure, which is a result of the fractures which create fissures for the fluid material points to infiltrate. In this example, we demonstrate that the fractures driven by the fluid pressure due to injection can be reasonably captured with the coupled total- and semi-Lagrangian PD formulations.

5. Conclusions and discussions

Presented in this paper is a peridynamics-based computational approach for modelling fluid-solid interactions and fluid-driven fractures by coupling the total- and semi-Lagrangian formulations. The former is used for modelling fracturing in solids, while the latter is employed for modelling fluids. A fictitious point-based FSI formulation is presented to model interactions between the fluid and solid. Benchmark models are presented for the dam break problem, crack profile under hydraulic pressure, and KGD hydraulic fracturing problem. A numerical simulation example is presented for injection-induced pressurization and fracturing in solid rock. The proposed computational approach is shown to reasonably simulate fluid flow, fluid-solid interactions, and fluid-driven fracturing in the solid, with comparison to experiments and analytical solutions.

The advantage of the coupled computational approach is that one does not need to explicitly describe the geometry of the fractures in modelling fluid-driven fracturing problems. This is appealing when considering cases where complex fracture patterns are expected to develop, and when the solid is unsaturated and impermeable such that fluid infiltration is dependant of the fractures. Nonetheless, the proposed approach is not without limitations. First, it is best suited for impermeable solid materials where fluid does not infiltrate

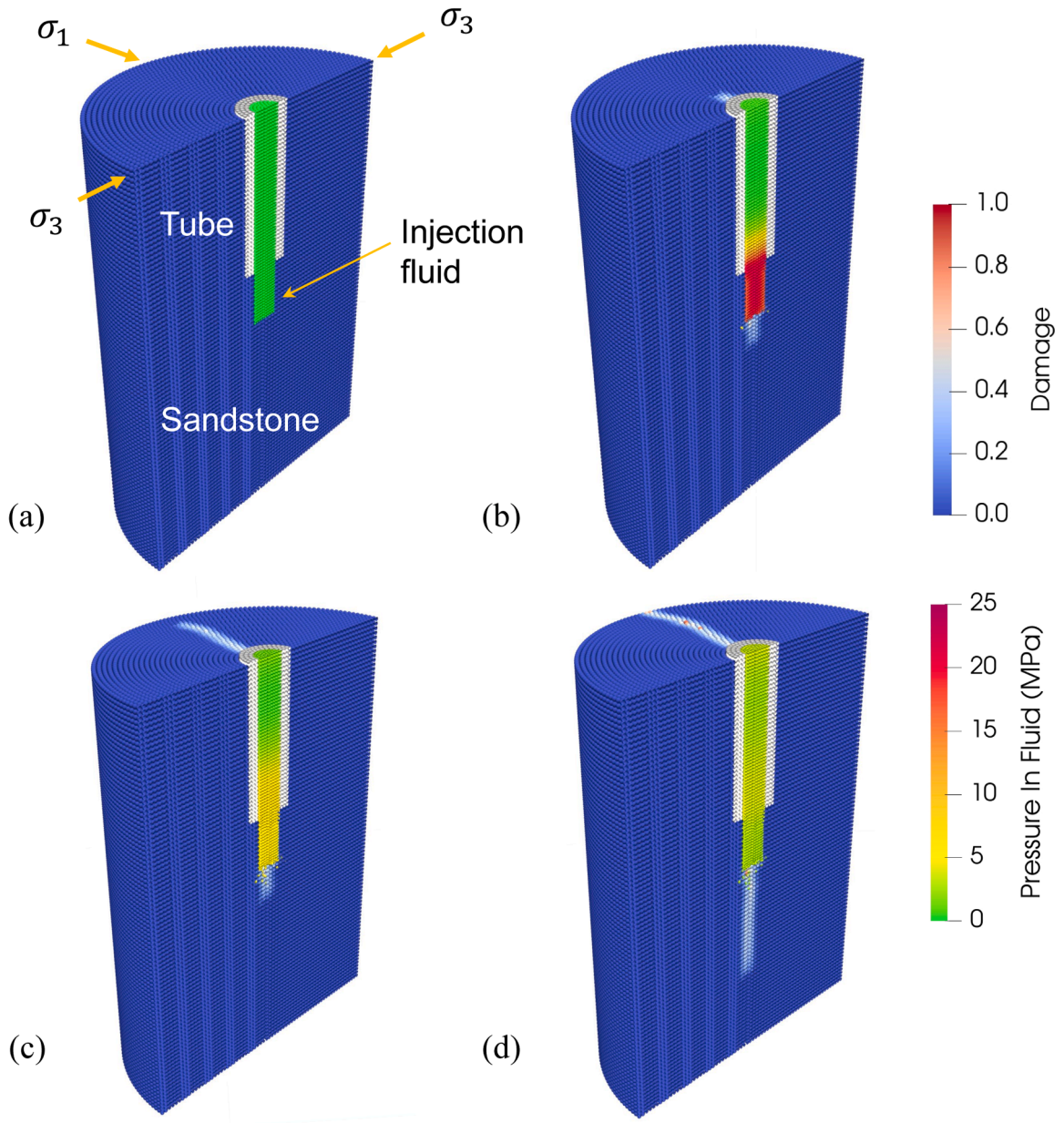

Fig. 16. Evolution of fluid pressure and progress of fracture in the sandstone. (a) initial condition; (b) at step 2000; (c) at step 4000; (d) at step 8000. The sandstone specimen is cut vertically at $x = 0$ for the purpose of presentation. The time that corresponds to (a) through (d) is marked in Fig. 18.

Table 4
Parameters for simulation of injection-induced brittle fracture in sandstone.

Parameters	Vegetable oil	Sandstone	Steel tube
Density: kg/m^3	900	2500	7800
Bulk modulus: GPa	1.5	2.72	100
Shear modulus: GPa	/	3.24	74
Poisson's ratio	/	0.37	0.3
Viscosity: Pa·s	5×10^{-3}	/	/
Fracture toughness: MPa·m$^{0.5}$	/	0.4	/
Critical energy release rate: J/m^2	/	22.9	/
$C_{PST} = 0.0$, $C_{RF} = 0.01$, $c_0 = 3580$ m/s, $n = 4.0$, $\delta = 3\Delta x$.			

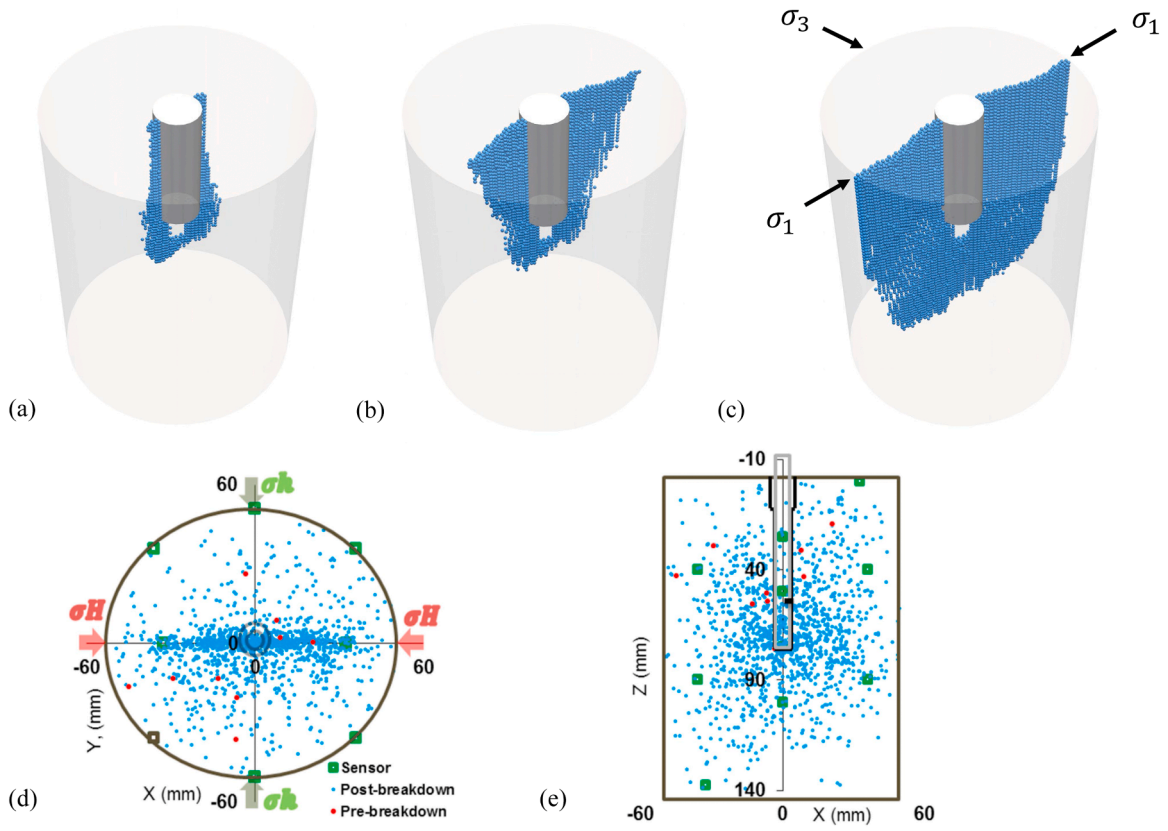

Fig. 17. Interior view of the fracture surfaces in the sandstone: (a) at step 2000; (b) at step 4000; (c) at step 8000; and acoustic emission events captured in experiment [61] in (d) top view; (e) side view. (For interpretation of the references to colour in this figure legend, the reader is referred to the web version of this article.)

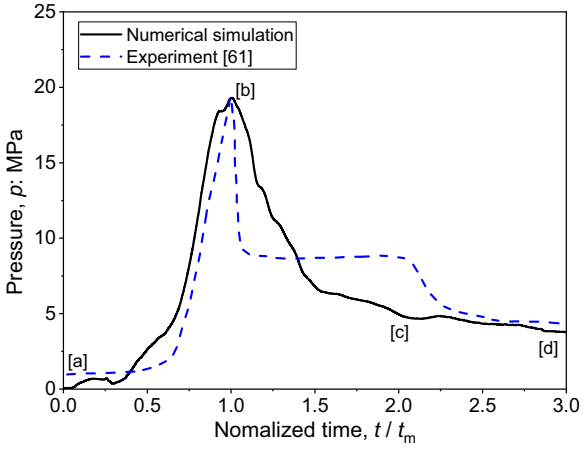

Fig. 18. Evolution of fluid pressure during injection and fracturing process. Conditions of the specimen at time [a] through [d] are shown in Fig. 16.

into solid. For porous solid material, additional consideration will be necessary to consider fluid diffusion into solid. Second, the application of the semi-Lagrangian-PD theory remains new and needs further efforts to extend it for larger scale simulation and potential engineering applications. It may also experience an unfavourable material instability issue [32], which should be addressed in future studies. Third, the computational cost associated with the coupled approach can be expensive if 3D simulation is performed for an endured fracturing and fluid infiltration process. This may be attributed to the nature of the semi-Lagrangian formulation which requires point neighbour to be updated each step. GPU based parallel computing may help for such cases. Moreover, it is worth noting

that the recently developed bond-associated PD theory [66–69] may also be considered in the modelling of solid and fluid. The theory has been found to offer good numerical stability while maintaining the versatility of the non-ordinary SBPD. The fluid-solid interaction model proposed herein will need to be further examined when used in conjunction with this recently developed PD theory.

Declaration of Competing Interest

The authors declare that they have no known competing financial interests or personal relationships that could have appeared to influence the work reported in this paper.

Data availability

No data was used for the research described in the article.

Acknowledgments

The study was financially supported by the National Science Foundation of China under project 11972030, Research Grants Council of Hong Kong (through GRF project 16208720 and CRF project C7082–22G, and HKUST SSTSP FP907), and Hetao Shenzhen-Hong Kong Science and Technology Innovation Cooperation Zone (HZQBKCZYB2020083). F. Zhu acknowledges support from JSPS KAKENHI Grant Number 23K13403. C. Yang acknowledges financial support from the Hong Kong Ph.D. Fellowship Scheme funded by Research Grants Council of Hong Kong and would also like to express gratitude to Prof. Dan Huang and Mr. Xuehao Yao from Hohai University and Dr. Haochen Chang from Tongji University for the beneficial discussions.

References

[1] L. Gandossi, U. Von Estorff, An Overview of Hydraulic Fracturing and Other Formation Stimulation Technologies For Shale Gas Production — Update 2015, Publications Office of the European Union, Luxembourg (Luxembourg), 2015, p. JRC98582. EUR 26347.
[2] M.H. Mosleh, M. Sedighi, M. Babaei, M. Turner, Geological sequestration of carbon dioxide, Manag. Glob. Warm. 2019 (2019) 487–500.
[3] E. Gordeliy, A. Peirce, Implicit level set schemes for modeling hydraulic fractures using the XFEM, Comput. Methods Appl. Mech. Engrg. 266 (2013) 125–143.
[4] N. Shauer, C.A. Duarte, A generalized finite element method for three-dimensional hydraulic fracture propagation: comparison with experiments, Eng. Fract. Mech. 235 (2020), 107098.
[5] S. Salimzadeh, N. Khalili, A three-phase XFEM model for hydraulic fracturing with cohesive crack propagation, Comput. Geotech. 69 (2015) 82–92.
[6] T. Mohammadnejad, A.R. Khoei, An extended finite element method for hydraulic fracture propagation in deformable porous media with the cohesive crack model, Finite Elem. Anal. Des. 73 (2013) 77–95.
[7] Q. Gao, Y. Cheng, S. Han, C. Yan, L. Jiang, Z. Han, J. Zhang, Exploration of non-planar hydraulic fracture propagation behaviors influenced by pre-existing fractured and unfractured wells, Eng. Fract. Mech. 215 (2019) 83–98.
[8] P. Gupta, C.A. Duarte, Coupled formulation and algorithms for the simulation of non-planar three-dimensional hydraulic fractures using the generalized finite element method, Int. J. Numer. Anal. Methods Geomech. 40 (2016) 1402–1437.
[9] Z. Sun, Z. Li, D.N. Espinoza, M.T. Balhoff, Fluid-driven fractures in granular media: insights from numerical investigations, Phys. Rev. E 101 (2020), 042903.
[10] J. Zhou, L. Zhang, A. Braun, Z. Han, Numerical modeling and investigation of fluid-driven fracture propagation in reservoirs based on a modified fluid-mechanically coupled model in two-dimentional particle flow code, Energies 9 (2016) 699.
[11] S. Gharehdash, M. Barzegar, I.B. Palymskiy, P.A. Fomin, Blast induced fracture modelling using smoothed particle hydrodynamics, Int. J. Impact Eng. 135 (2020), 103235.
[12] R. Pramanik, T. Douillet-Grellier, K. Pan, B.D. Jones, A. Albaiz, J.R. Williams, J. Du, H. Pourpak, D. Deb, An SPH approach to the simulation of hydraulic fracture propagation in naturally fractured rock medium, in: The 50th U.S. Rock Mechanics/Geomechanics Symposium, Houston, Texas, 2016. June 2016.
[13] S. Nadimi, I. Miscovic, J. McLennan, A 3D peridynamic simulation of hydraulic fracture process in a heterogeneous medium, J. Petrol Sci. Eng. 145 (2016) 444–452.
[14] S. Oterkus, E. Madenci, E. Oterkus, Fully coupled poroelastic peridynamic formulation for fluid-filled fractures, Eng. Geol. 225 (2017) 19–28.
[15] Y. Zhang, D. Huang, Z. Cai, Y. Xu, An extended ordinary state-based peridynamic approach for modelling hydraulic fracturing, Eng. Fract. Mech. 234 (2020), 107086.
[16] J. Adachi, E. Siebrits, A. Peirce, J. Desroches, Computer simulation of hydraulic fractures, Int. J. Rock Mech. Min. Sci. 44 (2007) 739–757.
[17] S.A. Silling, Reformulation of elasticity theory for discontinuities and long-range forces, J. Mech. Phys. Solids 48 (1) (2000) 175–209.
[18] S.A. Silling, M. Epton, O. Weckner, J. Xu, A. Askari, Peridynamics states and constitutive modelling, J. Thermoelasticity 88 (2) (2007) 151–184.
[19] W. Gerstle, N. Sau, S. Silling, Peridynamic modeling of concrete structures, Nucl. Eng. Des. 237 (12–13) (2007) 1250–1258.
[20] B. Kilic, E. Madenci, Prediction of crack paths in a quenched glass plate by using peridynamic theory, Int. J. Fracture 156 (2) (2009) 165–177.
[21] F. Zhu, J. Zhao, A peridynamic investigation on crushing of sand particles, Géotechnique 69 (6) (2019) 526–540.
[22] X.P. Zhou, X.D. Shou, Numerical simulation of failure of rock-like material subjected to compressive loads using improved peridynamic method, Int. J. Geomech. 17 (3) (2017), 04016086.
[23] Y.J. Gui, Y. Yu, Y.L. Hu, Y.T. Zhang, L.W. Lei, A peridynamic cohesive zone model for composite laminates, J. Peridynam. Nonlocal. Model. 3 (2021) 383–409.
[24] P. Diehl, S. Prudhomme, M. Levesque, A review of benchmark experiments for the validation of peridynamics models, J. Peridynam. Nonlocal. Model. 1 (2019) 14–35.
[25] M. Behzadinasab, G. Moutsanidis, N. Trask, J.T. Foster, Y. Bazilevs, Coupling of IGA and peridynamics for air-blast fluid-structure interaction using an immersed approach, Forces Mech 4 (2021), 100045.
[26] M. Behzadinasab, M. Hillman, Y. Bazilevs, IGA-PD penalty-based coupling for immersed air-blast fluid–structure interaction: a simple and effective solution for fracture and fragmentation, J. Mech. 37 (2021) 680–692.
[27] S. Shende, M. Behzadinasab, G. Moutsanidis, Y. Bazilevs, Simulating air blast on concrete structures using the volumetric penalty coupling of isogeometric analysis and peridynamics, Math. Models Methods Appl. Sci. 32 (12) (2022) 2477–2496.
[28] F. Yang, X. Gu, X. Xia, Q. Zhang, A peridynamics-immersed boundary-lattice Boltzmann method for fluid-structure interaction analysis, Ocean Eng. 264 (2022), 112528.
[29] H. Fan, G.L. Bergel, S. Li, A hybrid Peridynamics-SPH simulation of soil fragmentation by blast loads of buried explosive, Int. J. Impact Eng. 87 (2016) 14–27.
[30] H. Fan, S. Li, A Peridynamics-SPH modeling and simulation of blast fragmentation of soil under buried explosive loads, Comput. Methods Appl. Mech. Engrg. 318 (2017) 349–381.

[31] X. Yao, D. Huang, Coupled PD-SPH modeling for fluid-structure interaction problems with large deformation and fracturing, Comput. Struct. 270 (2022), 106847.
[32] S.A. Silling, M.L. Parks, J.R. Kamm, O. Weckner, M. Rassaian, Modeling shockwaves and impact phenomena with Eulerian peridynamics, Int. J. Impact Eng. 107 (2017) 47–57.
[33] M. Behzadinasab, J.T. Foster, A semi-Lagrangian constitutive correspondence framework for peridynamics, J. Mech. Phys. Solids 137 (2020), 103862.
[34] G.L. Bergel, S. Li, The total and updated lagrangian formulations of state-based peridynamics, Comput. Mech. 58 (2016) 351–370.
[35] Q. Tu, S. Li, An updated Lagrangian particle hydrodynamics (ULPH) for Newtonian fluids, J. Comput. Phys. 348 (2017) 493–513.
[36] J. Yan, S. Li, A.M. Zhang, X. Kan, P.N. Sun, Updated Lagrangian Particle Hydrodynamics (ULPH) modeling and simulation of multiphase flows, J. Comput. Phys. 393 (2019) 406–437.
[37] F. Zhu, J. Zhao, Peridynamic modelling of blasting induced rock fractures, J. Mech. Phys. Solids 153 (2021), 104469.
[38] E. Madenci, A. Barut, M. Futch, Peridynamic differential operator and its applications, ComputMethods Appl. Mech. Eng. 304 (2016) 408–451.
[39] Y. Gao, S. Oterkus, Nonlocal numerical simulation of low Reynolds number laminar fluid motion by using peridynamic differential operator, Ocean Eng. 179 (2019) 135–158.
[40] Y. Gao, S. Oterkus, Multi-phase fluid flow simulation by using peridynamic differential operator, Ocean Eng. 216 (2020), 108081.
[41] Y. Gao, S. Oterkus, Fluid-elastic structure interaction simulation by using ordinary state-based peridynamics and peridynamic differential operator, Eng. Anal. Bound Elem. 121 (2020) 126–142.
[42] S.A. Silling, E. Askari, A meshfree method based on the peridynamic model of solid mechanics, Comput. Struct. 83 (2005) 1526–1535, 17–18.
[43] M.B. Liu, G.R. Liu, Particle Methods for Multi-Scale and Multi-Physics, World Scientific Publishing Co. Inc, 2016.
[44] J.J. Monaghan, Simulating free surface flows with SPH, J. Comput. Phys. 110 (2) (1994) 399–406.
[45] R. Xu, P. Stansby, D. Laurence, Accuracy and stability in incompressible SPH (ISPH) based on the projection method and a new approach, J. Comput. Phys. 228 (18) (2009) 6703–6725.
[46] Z.L. Zhang, K. Walayat, J.Z. Chang, M.B. Liu, Meshfree modeling of a fluid-particle two-phase flow with an improved SPH method, J. Numer. Meth. Eng. 116 (8) (2018) 530–569.
[47] J.J. Monaghan, A. Kos, N. Issa, Fluid motion generated by impact, J. Waterw., Harbors Coastal Eng. Div., Am. Soc. Civ. Eng. 129 (6) (2003) 250–259, port, coastal, and ocean engineering.
[48] G.K. Batchelor, An Introduction to Fluid Dynamics, Cambridge university press, 1967.
[49] H.C. Chang, A.R. Chen, A. Kareem, L. Hu, R.J. Ma, Peridynamic differential operator-based Eulerian particle method for 2D internal flows, Comput. Methods Appl. Mech. Engrg. 392 (2022), 114568.
[50] S. Koshizuka, Y. Oka, Moving-particle semi-implicit method for fragmentation of incompressible fluid, Nucl. Sci. Tech. 123 (3) (1996) 421–434.
[51] S. Koshizuka, A particle method for incompressible viscous flow with fluid fragmentation, Comput. Fluid Dyn. J. 4 (1995) 29.
[52] J.C. Martin, W.J. Moyce, W.G. Penney, A.T. Price, C.K. Thornhill, Part IV. An experimental study of the collapse of liquid columns on a rigid horizontal plane, Philos. Trans. A Math. Phys. Eng. Sci 244 (882) (1952) 312–324.
[53] I. Sneddon, The distribution of stress in the neighbourhood of a crack in an elastic solid, Proc. Math Phys. Eng. Sci. 187 (1946) 229–260.
[54] J. Geertsma, F. De Klerk, A rapid method of predicting width and extent of hydraulically induced fractures, J. Pet. Technol. 21 (12) (1969) 1571–1581.
[55] A.P. Bunger, E. Detournay, D.I. Garagash, Toughness-dominated hydraulic fracture with leak-off, Int. J. Fracture 134 (2005) 175–190.
[56] M.R.M. Aliha, A. Bahmani, S. Akhondi, Mixed mode fracture toughness testing of PMMA with different three-point bend type specimens, Eur. J. Mech. A. Solids 58 (2016) 148–162.
[57] D.I. Garagash, Propagation of a plane-strain hydraulic fracture with a fluid lag: early-time solution, Int. J. Solids Struct. 43 (18–19) (2006) 5811–5835.
[58] B. Lecampion, E. Detournay, An implicit algorithm for the propagation of a hydraulic fracture with a fluid lag, Comput. Methods Appl. Mech. Engrg. 196 (49–52) (2007) 4863–4880.
[59] M.J. Hunsweck, Y. Shen, A.J. Lew, A finite element approach to the simulation of hydraulic fractures with lag, Int. J. Numer. Anal. Methods Geomech. 37 (9) (2013) 993–1015.
[60] H.L. Ren, X.Y. Zhuang, Y.C. Cai, T. Rabczuk, Dual-horizon peridynamics, Int. J. Numer. Meth. Eng 108 (12) (2016) 1451–1476.
[61] S.M. Patel, C.H. Sondergeld, C.S. Rai, Laboratory studies of hydraulic fracturing by cyclic injection, Int. J. Rock Mech. Min. Sci. 95 (2017) 8–15.
[62] M.L. Parks, D.J. Littlewood, J.A. Mitchell, S.A. Silling, Peridigm users' Guide, Sandia National Laboratories, Sandia Report. Albuquerque, NM, USA, 2012.
[63] R.J. Cuss, An experimental investigation of the mechanical behaviour of sandstones with reference to borehole stability. PhD thesis, University of Manchester, 1998.
[64] B.K. Atkinson, Fracture toughness of Tennessee Sandstone and Carrara marble using the double torsion testing method, Int. J. Rock Mech. Min. Sci. Geomech. Abstr. 16 (1979) 49–53.
[65] A.J. Rostocki, D.B. Tefelski, S. Ptasznik, Compressibility studies of some vegetable oils up to 1 GPa, High Press Res. 29 (4) (2009) 721–725.
[66] T. Breitzman, K. Dayal, Bond-level deformation gradients and energy averaging in peridynamics, J. Mech. Phys. Solids 110 (2018) 192–204.
[67] H. Chen, Bond-associated deformation gradients for peridynamic correspondence model, Mech. Res. Commun. 90 (2018) 34–41.
[68] M. Behzadinasab, J.T. Foster, Revisiting the third Sandia Fracture Challenge: a bond-associated, semi-Lagrangian peridynamic approach to modeling large deformation and ductile fracture, Int. J. Fract. 224 (2) (2020) 261–267.
[69] Y. Bazilevs, M. Behzadinasab, J.T. Foster, Simulating concrete failure using the microplane (M7) constitutive model in correspondence-based peridynamics: validation for classical fracture tests and extension to discrete fracture, J. Mech. Phys. Solids 166 (2022), 104947.